ORIGINAL PAPER

Low voltage electroosmotic pump for high density integration into microfabricated fluidic systems

Friedjof C. A. Heuck · Urs Staufer

Abstract A low voltage electroosmotic (eo) pump suitable for high density integration into microfabricated fluidic systems has been developed. The high density integration of the eo pump required a small footprint as well as a specific on-chip design to ventilate the electrolyzed gases emerging at the platinum (Pt) electrodes. For this purpose, a novel liquid–gas (lg) separator was invented. This lg-separator separated the gas bubbles from the liquid and guided them away from the eo pump. Its operational principle was solely based on the geometry of tapered sidewalls. An eo pump sandwiched by two lg separators (microchannels in the range of 10 μm, footprint of 100 μm × 15 μm) was experimentally investigated. The lg-separator was able to reliably separate and ventilate an emerging gas flow of 2 pl s^{-1}. The eo pump achieved flow rates of 50 pl s^{-1} at actuation voltages of 5 V.

Keywords Electroosmosis · Microfluidic · Gas–liquid interface · Micropump

1 Introduction

Electroosmotic (eo) pumps have attracted considerable attention within the recent years (Ghosal 2004; Laser and Santiago 2004; Morf et al. 2001; Guenat et al. 2001; Seibel et al. 2008; Brask et al. 2005; Hug et al. 2005; Takamura

et al. 2003), due to their ability to provide pulsation free flow without any moving parts. These active electrically controlled pumps are highly suitable for the integration into complex fluidic systems (Seibel et al. 2008). A key challenge of the design of eo pumps is the coupling of the electrical current into the ionic solution, which is commonly done with electrodes made out of Pt. However, in that case, the electron transfer is linked to electrolyzing the solvent and gases are formed. These gases emerge as bubbles and may block the conductive liquid-path between the electrodes and, hence, inhibit a further actuation of the pump. Furthermore, once a gas bubble is fully developed and stretches out over the complete microchannel cross-section, they become almost immobile, since in these dimensions, capillary forces from the liquid–gas interface are the dominate force. It is, therefore, imperative to keep these bubbles away from the eo pump and the functional liquid part of the fluidic system.

Several methods to avoid mixing the electrolyzed gases with the functional fluidic system have been investigated and reported in literature. Brask et al. (2005) used a hybrid approach for the current coupling by assembling an ion exchange membrane between the electrodes and the eo active microchannel. These membranes were permeable for the ionic current and reliably stopped the electrolyzed gases to enter the fluidic system. In order to omit bulky fluidic connections or a membrane, Hug et al. (2005) used a design of different electrical resistances within the fluidic system. In their work, the electrodes were placed into top open reservoirs which were connected to wide microchannels. These wide microchannels connected the sub-micron wide eo pump. A voltage drop between the electrodes led to a proportionally large voltage drop over the eo pump, due to its comparatively large electrical resistance. Another approach of omitting bulky fluidic

F. C. A. Heuck · U. Staufer
Micro and Nanoengineering Laboratory, 3mE, Delft University of Technology, Mekelweg 2, 2628 CD Delft, The Netherlands

F. C. A. Heuck (✉) · U. Staufer
DIMES, Delft University of Technology, Feldmannweg 17, 2628 CT Delft, The Netherlands
e-mail: f.c.a.heuck@tudelft.nl

connections and thus allowing further miniaturizing of the eo pump was the integration of photocurable gel inside the fluidic system, as shown by Takamura et al. (2003). This photocurable gel served as a salt bridge towards Ag/AgCl electrodes, which avoided gas bubbles formation. This process allowed a miniaturization but it required the more complex integration of a photocurable gel.

All the above mentioned eo pump designs avoided the interaction of liquid and gas inside the microchannels. For cases, where gas and liquid do get into direct contact inside microchannels, strategies to handle and separate segmented liquid–gas flows have been developed (Guenther et al. 2005), which might be adapted to the situation of the eo pump. A theoretical description of gas bubbles inside microchannel constrictions has been presented by Jensen et al. (2004). In their work, it is mentioned that such constrictions exert considerable Young–Laplace pressure on gas bubbles. Paust et al. (2009) used a version formed by tapered microchannel sidewalls to passively guide gases for direct methanol fuel cells. With the current solutions, a high density integration of eo pumps into microfluidic systems is not possible. A design suitable for the same purpose in the case of an eo micropump, its implementation and analysis is presented in this paper. The mixing of electrolyzed gases within the functional fluidic system is avoided by a novel concept of a liquid–gas (lg) separator. This lg-separator is placed between the electrodes and the eo pump and it drives the emerging gas bubbles away via an exhaust microchannel. The strong capillary forces from the liquid–gas interface in the micrometer ranged microchannels enable the lg-separator to reliably work solely by its geometry.

This paper is structured as follows: a model of the eo pump embedded in a fluidic system is developed. In detail, the physical background of the lg-separator is explained. Then, the model of the lg-separator is assembled together with the eo pump and the connecting microchannels to a fluidic system. In order to extract the relevant design parameters for the fabrication, the pressures and flows within the fluidic system are determined. Finally, the eo fabrication process for the eo pump is outlined and the experimental validation of the design is presented.

2 Electroosmotic pump with liquid–gas-separator

2.1 Model of the liquid–gas-separator

2.1.1 Geometry of the liquid–gas-separator and general assumptions

The lg-separator consisted of a tapered sidewall and an electrode integrated into the bottom of the microchannel, as

shown in Fig. 1. It is integrated into the fluidic system with its narrow side, the inlet, oriented towards the eo pump and with its larger side, the outlet, facing the exhaust. The electrode of the eo pump, at which the gas bubble forms, is located inside the lg-separator. This bubble is geometrically confined by the bottom and the sidewalls. It will be shown in the following section that in a tapered microchannel the bubble moves towards the wider side and, hence, away from the electrode. The bubble growth is analytically described in three dimensions. Behind the electrode pointing towards the outlet of the lg-separator, the bubble may stretch over the complete cross-section of the microchannel and may touch the top. At this moment, the water column within the microchannel is separated and any pressure change between the inlet and the outlet of the lg-separator acts directly on the bubble, respectively, on their two separate menisci. The lg-separator compensates for these external pressure changes by its backpressure. In order to model the backpressure, it is assumed that the microchannel is much higher than wide and, hence, the curvature of the meniscus is completely defined by the width (Han et al. 2006), which reduces the model to two dimensions.

The formation and movement of the gas bubbles was modeled in a quasi static approximation. In addition, the processes were assumed to be isothermal, since any heat would be quickly removed by thermal conduction through the surrounding bulk silicon (Si). The following parameters were used in the model: the viscosity of the liquid (water) $\eta = 1$ mPas and the surface tension of the water–air interface $\gamma_{la} = 73$ mJ m^{-2}. The contact angle for the
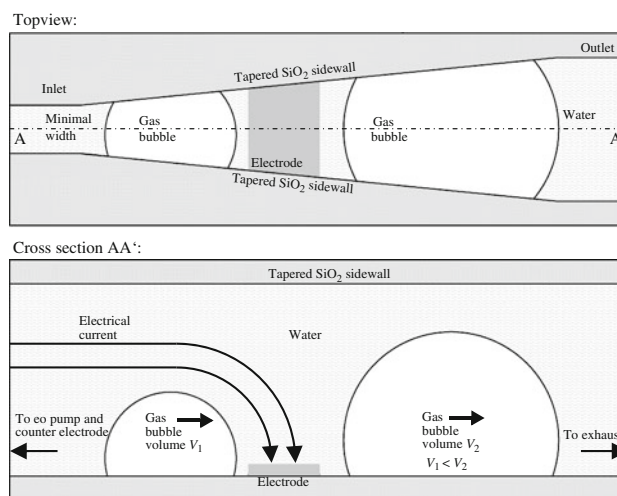

Fig. 1 Sketch of the lg-separator. It enables the coupling of electrical current into the solution and the separation of the emerging electrolyzed gas bubbles from the functional liquid fluidic system. Its operation is based on tapered sidewalls which drive the electrolyzed gas bubbles with increasing bubble volume away from the electrode towards the exhaust

silicon dioxide (SiO$_2$) microchannel and water was measured under static conditions to be $\theta_s = 45°$. The contact angle hysteresis for the observed flow rates over the thermally grown SiO$_2$ surfaces was measured to be 5°, i.e., a receding contact angle of $\theta_r = 42°$ and advancing contact angle of $\theta_a = 47°$.

2.1.2 Bubble development at the electrode

Electrolysis initiates the bubble growth at the electrode. Assuming that the electrolyzed gas conserves its internal energy U_{int}, according to the ideal gas law, enables us to define its internal pressure p_{int} and its volume V

$$U_{int} = p_{int}V. \tag{1}$$

In the absence of any external pressures, the internal pressure p_{int} needs to match the Young–Laplace pressure p_c, $p_{int} = p_c$, which describes the effect of the liquid gas surface tension γ_{la} confining the liquid–gas interface of the bubble. Due to the properties of a liquid, the shape of the liquid–gas interface is spherical with the radius R. The capillary Young–Laplace pressure p_c can then be described by

$$p_c = \frac{\gamma_{la}}{R}. \tag{2}$$

At the bottom, the bubble encounters the transition between three different interfacial energies, the solid–liquid, the liquid–air, and the solid–air interfacial energy. At this intersection, Young's equation demands that the angle enclosed by the tangent of the liquid–gas interface and the bottom equals the static contact angle θ_s. Figure 2a shows the spherical bubble at the bottom of the microchannel. The z coordinate defines the distance from the bottom of the microchannel. The height of the bubble center is $R_h = R \cos \theta_s$. Figure 2b shows the horizontal cross-section of the

spherical bubble in its center. Due to symmetry, the bubble's horizontal center is also in the horizontal center of the microchannel. The bubble center's distance R_w from the tapered sidewall is defined as $R_w = w \cos \beta$, where w is half of the microchannel width and β the taper angle of the microchannel. The taper of the microchannel is defined as $w = w_0 + x \tan \beta$, where w_0 and x denote half of the initial microchannel width at the electrode and the distance of the bubble center from the electrode, respectively. The direction x is defined to origin at the smaller edge of the electrode and to point towards the outlet of the lg-separator.

This initial bubble B_0 can grow until it touches the tapered microchannel sidewall. Its radius R_0 then equals the distance between the center of the bubble and the sidewall $R_0 = w_0 \cos \beta$ at the smaller side of the electrode $x_0 = 0$. The internal energy U_0 of the initial bubble B_0 can be calculated to

$$U_0 = p_0 V_0 = \frac{\gamma_{la}}{R_0} \int_{-R_0}^{R_0 \cos \theta_s} \int_0^{2\pi} \int_0^{\sqrt{R_0^2 - z^2}} r\,\mathrm{d}r\,\mathrm{d}\omega\,\mathrm{d}z. \tag{3}$$

As soon as, the initial bubble B_0 touches the sidewall, two more transition points between three different interfacial energies occur, at which the Young's boundary condition requires the contact angle θ_s. Hence, the bubble needs to change its shape to a new first bubble B_1 and as a consequence its position $x_0 \to x_1$ shifts within the microchannel. Figure 3a shows the geometry of the first bubble. The shape of the first bubble B_1 remains spherical, due to the absence of any external pressures. The radius R_1 of the first bubble can be calculated to

$$R_1 = \frac{R_w}{\cos \theta_s} = (w_0 + x \tan \beta) \cos \beta \sec \theta_s \tag{4}$$

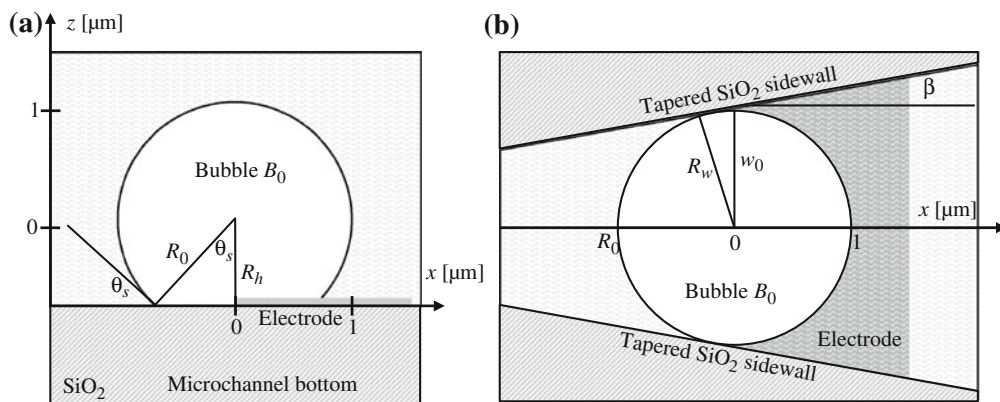which defines the first bubble's B_1 internal energy U_1 to

Fig. 2 Sketch of the spherical initial bubble B_0. **a** Vertical cross-section through bubble center revealing the height of the bubble center R_h. **b** Horizontal cross-section through bubble center revealing the maximum radius of the initial bubble $R_0 = R_w$. In this sketch, the initial opening $w_0 = 1$ μm, the taper angle $\beta = 10°$ and the static contact angle $\theta_s = 45°$
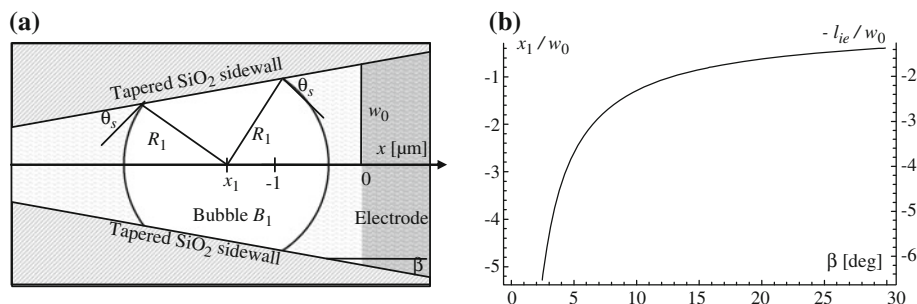
(a)

(b)

Fig. 3 a Horizontal cross-section of the first bubble B_1 through its center. It reveals the new bubble radius R_1 and its position within the microchannel x_1. In this sketch, the initial opening $w_0 = 1$ μm, the taper angle $\beta = 10°$ and the static contact angle $\theta = 45°$. **b** On the left ordinate the position x_1 of the first bubble B_1 and on the right ordinate the minimum distance from the electrode to the inlet of the lg-separator is shown as a function of the taper angle β

$$U_1 = \frac{\gamma_{la}}{R_1}\left(\int\limits_{-R_1}^{R_1 \cos\theta_s} \int\limits_0^{2\pi} \int\limits_0^{\sqrt{R_0^2-z^2}} r\,dr\,d\omega\,dz \right.$$

$$\left. -2 \int\limits_{R_1 \cos\theta_s}^{R_1} \int\limits_0^{2\pi} \int\limits_0^{\sqrt{R_0^2-z^2}} r\,dr\,d\omega\,dz \right). \tag{5}$$

This transition from the initial bubble B_0 to the first bubble B_1 is considered to be isothermal. Moreover, the bubble positions and deforms itself faster than new gas is generated by electrolysis. The rate of the gas development can be adjusted by the applied current and this can be chosen small enough to fulfill this criteria, and hence, the bubble can be considered as a closed system during this short transition phase. According to the ideal gas law, the internal energy U_{int} then remains constant

$$U_{int} = U_0 = U_1. \tag{6}$$

Inserting Eqs. 3 and 5 into Eq. 6, replacing the radius R_1 with Eq. 4, and solving of the first bubble's center position $x = x_1$ yields

$$x_1 = w_0 \cot\beta \left(\sqrt{\frac{\left(\cos\frac{\theta_s}{2}\right)^4 (\cos\theta_s - 2)}{3\cos\theta_s + \sec\theta_s(2\sec\theta_s - 9)}} - 1 \right) \tag{7}$$

Since the square root is less than 1 for $0 < \theta_s < \pi/2$, the bubble clearly detaches from the electrode and jumps into its new position $x_1 < 0$. This is illustrated in Fig. 3a where a horizontal cross-section through the center of the first bubble B_1 is shown. This shift in position needs to be considered for the placement of the electrode within the lg-separator. The bubble may not escape through the inlet of the lg-separator into the eo pump. The following effects may influence this movement: pinning of the gas bubble, as experienced in the work by Paust et al. (2009), might delay the positioning of the bubble from its initial position. Such

delay results in a larger bubble volume which leads to a shorter leap into the microchannel constriction. The same accounts for the contact angle hysteresis: the lower the receding contact angle θ_r and the larger the advancing contact angle θ_a, the shorter the leap into the microchannel constriction. Within the experiments, no delay or complete pinning could be observed, the bubble detached smoothly from the electrode. The contact angle hysteresis was observed and measured as indicated above ($\theta_r = 42°$, $\theta_a = 47°$, $\theta_s = 45°$). Therefore, we selected to work with the assumption of static conditions which represents a worst case scenario.

The position of the first bubble's center x_1 as a function of the taper angle β is shown in Fig. 3b. It can be seen that for small taper angles β the position x_1 of the first bubble reaches far into the narrow part of the microchannel. The maximum distance of the bubble's liquid–gas interface into the lg-separator is the same as the minimum distance l_{ie} from the inlet of the lg-separator to the electrode. By the geometry, the minimum distance l_{ie} can be calculated to

$$l_{ie} > w_0 \left(\cot\beta + (\cos\beta\sec\theta_s - \cot\beta) \right.$$

$$\left. \times \sqrt{\frac{\left(\cos\frac{\theta_s}{2}\right)^4 (\cos\theta_s - 2)}{3\cos\theta_s + \sec\theta_s(2\sec\theta_s - 9)}} \right) \tag{8}$$

The minimum distance l_{ie} to the inlet of the lg-separator is shown Fig. 3b, on the right ordinate axis.

2.1.3 Bubble movement within the liquid–gas-separator

During the electrolysis, continuously more bubbles start to grow at the electrode. These bubbles merge with the first bubble B_1, once their liquid–gas interfaces touch each other. This lets the first bubble B_1 grow and move towards the electrode and then past the electrode and finally out of the lg-separator. During this movement, it is important that the bubble does not disconnect or strongly constrain

the electrical path between the electrodes, which would stop the eo pumping. This might occur in two different ways. First, the bubble may cover the electrode completely, hence, a minimum electrode length l_e is required for preventing this, and second, the bubble stretches out over the complete cross-section and reaches the top, hence, a minimum height h_c of the microchannel is required. Figure 4 shows the situation of the critical bubble B_c, which occurs once the bubble's smaller liquid air meniscus just touches the small side of the electrode on the microchannel bottom. The liquid–gas interface has a circular shape of R_b at the bottom of the microchannel. By geometry, $R_b = w_0/\cos(\theta_s + \beta)$, and the minimum electrode length l_e equates to

$$l_e > 2R_b \sin(\beta + \theta_s) = 2w_0 \tan(\beta + \theta_s). \quad (9)$$

For the minimum height h_c, the radius R_c of the critical bubble is needed and can be determined by geometrical considerations to $R_c = R_b/\sin\theta_s$. From this, the minimum height of the microchannel is

$$h_c = R_c(1 + \cos\theta_s) = w_0 \sec(\theta_s + \beta)[\cot\theta_s + \csc\theta_s] \quad (10)$$

The minimum electrode length l_e and the minimum microchannel height h_c as a function of the taper angle β is shown Fig. 5. It can be seen that large taper angles β
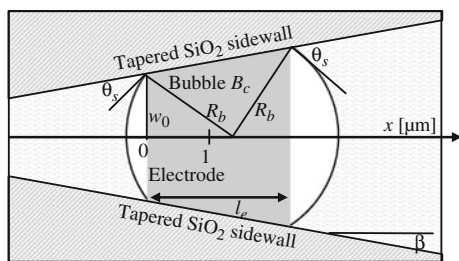

Fig. 4 Sketch of the critical bubble at the bottom of the microchannel. From this sketch the minimum electrode length l_e can be determined. In this sketch, the initial opening $w_0 = 1$ μm, the taper angle $\beta = 10°$ and the static contact angle $\theta_s = 45°$

enforce an even larger electrode length l_e and a larger minimum microchannel height h_c.

2.1.4 Backpressure of the liquid–gas-separator

During further actuation, the bubble in the outlet section of the lg-separator grows further and eventually stretches out over the complete cross-section. At this moment, the bubble separates the water column inside the microchannel into two detached liquid–gas interfaces, i.e., into two different menisci. Any pressure difference between the inlet and the outlet of the lg-separator acts directly on the bubble and displaces its respective menisci. In order to still reliably couple the current into the solution, the bubble may not be driven back over or behind the electrode, which could happen if the pressure on the meniscus facing the outlet exceeds the one acting on the other meniscus from the other side by a threshold value. This threshold is built up by the Young–Laplace pressure of the two separate menisci, and it can be considered as the backpressure tolerance p_b of the lg-separator. In order to calculate this backpressure p_b, it is assumed that the microchannel is much higher than wide and, hence, the curvature of the meniscus is completely defined by the width (Han et al. 2006) which reduces the model to two dimensions. In this first assumption, also any shape deformation of the meniscus's liquid–gas interfaces by the rectangular corners, connecting the microchannel sidewall to the top and the bottom, respectively, is neglected. The bubble can then be represented by the two separated menisci, as shown in Fig. 6. The dependency of the backpressure p_b on the initial microchannel width w_0 and the taper angle β are best explained by setting the initial opening w_0 at the position x_1 of the first meniscus and define the position of the second meniscus by the bubble length l_b. Since the bubble is pushed out of the capillary the contact angle hysteresis needs to be considered (Paust et al. 2009), this results in an advancing contact angle θ_a for the first meniscus and a
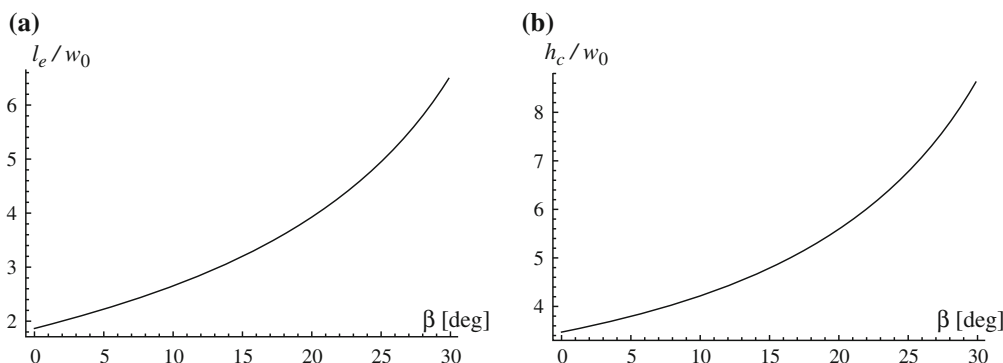

Fig. 5 **a** The dimensions of the critical bubble B_c determine the minimum electrode length l_e and the minimum microchannel height h_c. **a** The minimum electrode length l_e and **b** the minimum microchannel height h_c as a function of the taper angle β

receding contact angle θ_r for the second meniscus. The Young–Laplace pressure drop p_1 and p_2 over the respective menisci can be calculated to

$$p_1 = \frac{\gamma_{la}}{R_1} = \gamma_{la}\frac{\cos(\theta_a + \beta)}{w_0} \quad \text{and} \quad (11)$$

$$p_2 = \frac{\gamma_{la}}{R_2} = \gamma_{la}\frac{\cos(\theta_r - \beta)}{w_0 + l_b \tan \beta}. \quad (12)$$

Furthermore, for the backpressure p_b the bubble length l_b is parameterized by the bubble parameter $b_p = l_b/w_0$ which leads to the backpressure as

$$p_b = p_1 + p_2 = \frac{\gamma_{la}}{w_0}\left[\cos(\theta_a + \beta) - \frac{\cos(\theta_r - \beta)}{1 + b_p \tan \beta}\right]. \quad (13)$$

As long as, p_b is positive, the bubble will be reliably conducted away. In order to generate high backpressures p_b, the initial width w_0 of the microchannel at the electrode should be chosen as small as possible. The choice of the optimal taper angle β is more complex. Figure 7a shows the backpressure p_b versus the parameterized bubble length b_p. For small parameterized bubble lengths b_p, the backpressure p_b becomes negative and the bubble moves to lower values of x. For taper angles $\beta > \pi/2 - \theta_a$, the backpressure p_b
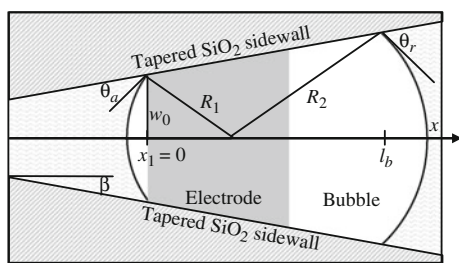

Fig. 6 Sketch of an horizontal cross-section showing the entrapped bubble stretched over the complete cross-section of the microchannel. The microchannel is cut along the symmetry line in its center. The sketch reveals the two menisci radii, R_1 and R_2 which are essential for the calculation of the lg-separator backpressure p_b

always stays negative, which represents a hydrophobic behavior of the microchannel. The backpressure p_b saturates for long bubbles in the Young–Laplace pressure p_1 of the first meniscus. The maximum bubble parameter b_{pmax} is limited by the distance l_{eo} of the electrode to the outlet of the lg-separator $b_{pmax} = l_{eo}/w_0$. Moreover, this assumes that the aspect ratio remains high towards the end of the lg-separator. The backpressure p_b versus the taper angle β is shown in Fig. 7b. The maximum backpressure p_b, reached by a specific taper angle β can be determined from the graph. The backpressure p_b raises steeply for small taper angles β and declines slowly for larger taper angles β. The value of the taper angle β for the maximum backpressure p_b at a receding contact angle θ_r of 42° and an advancing contact angle θ_a of 47° stays below a taper angle β of 12° for all bubble lengths.

2.1.5 Summary of the design parameters for the liquid–gas-separator

Figure 8 shows an lg-separator with its design critical lengths. The microchannel width w_0 at the electrode and the taper angle β should be chosen in order to guarantee a reproducible fabrication and a high backpressure p_b of the lg-separator to reliably conduct the electrolyzed gases away. From the above mentioned considerations, the smallest possible microchannel width w_0 should be chosen since all critical design values and the backpressure p_b scale with the inverse of the width w_0. In addition a taper angle β of 10° represents a good choice. With this taper angle β, the electrode should be placed according to: the distance of the electrode to the inlet of the lg-separator l_{ie} is about w_0, see Eq. 8 and Fig. 3b. The minimum length of the electrode l_e is about 4 w_0, see Eq. 9 and Fig. 5a. The distance of the electrode to the outlet of the lg-separator l_{eo} is about 20 w_0, see Eq. 13 and Fig. 7. The microchannel should have a minimum height h_c of about 5 w_0, see Eq. 10 and Fig. 5b.
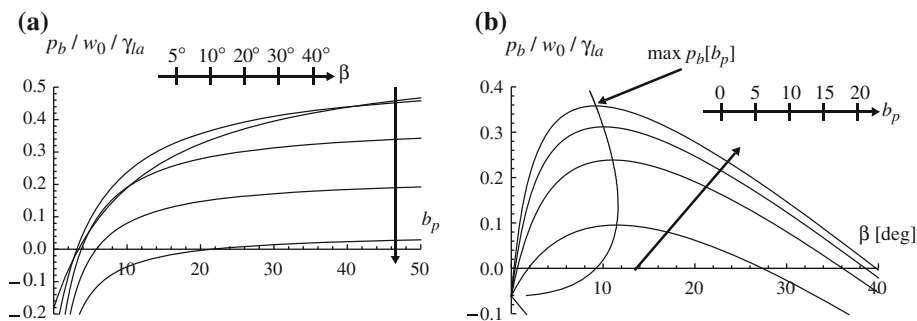

Fig. 7 a The lg-separator backpressure p_b as a function of the bubble parameter. A minimum bubble length is required to have a positive backpressure p_b. At long bubble lengths the backpressure p_b saturates to the Young–Laplace pressure of the first meniscus. The smaller the taper angle β, the higher the saturation backpressure p_b. **b** The

backpressure p_b as a function of the taper angle β. At small taper angles β the backpressure p_b steeply increases until it reaches its maximum. This maximum is reached, for an receding contact angle $\theta_r = 42°$ and an advancing contact angle $\theta_a = 47°$ and for a taper angle $\beta < 12°$ for all bubble lengths
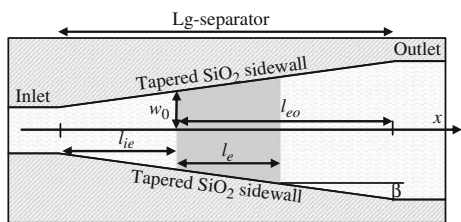
Fig. 8 Sketch of the lg-separator showing its critical dimensions. The microchannel sidewall has the opening of w_0 at the electrode. The microchannel sidewall is tapered with the angle β. The electrode has the length l_e. The small electrode edge has a distance l_{ie} from the inlet and a distance l_{eo} from the outlet

2.2 Model of the fluidic system with an embedded electroosmotic pump

A sketch of a fluidic system with an embedded eo pump is shown in Fig. 9a. The chip is fluidically contacted via large reservoirs (capacity 0.2 μl). Within the chip, the eo pump is fluidically contacted by the pump inlet and pump outlet microchannel and electrically contacted via the electrodes placed inside an lg-separator.

2.2.1 Filling of the fluidic system and operation of the electroosmotic pump

In order to derive the boundary conditions for the modeling, the filling and the operation of the eo pump needs to be taken into account. For the experiment, a droplet of aqueous solution was placed in the reservoir of the pump inlet and outlet. The Pt electrodes were connected through the contact pads, which were situated in the opening of the exhaust microchannel. By applying a voltage between the two electrodes, a current was coupled into the solution. This started the electrolysis and the lg-separator conducted the emerging gas out of the exhaust microchannel. At the same time, the current coupled into the solution led to: a proportionally small voltage drop over the first electrode inside the lg-separator and the pump inlet, a proportionally larger voltage drop over the eo pump, and a proportionally small voltage drop from the pump outlet to the second electrode, in the second lg-separator. These voltage drops induced eo pressures and thereby induced a flow through the inlet microchannel towards the pump, as well as, a flow out of the pump into the outlet microchannel.

2.2.2 Flow determination within the fluidic system

Next to the eo induced flow the model needs to integrate the influence of evaporation driven flow through the exhaust microchannel, hydrostatic pressure induced flow, and flow induced due to misalignment of the electrodes
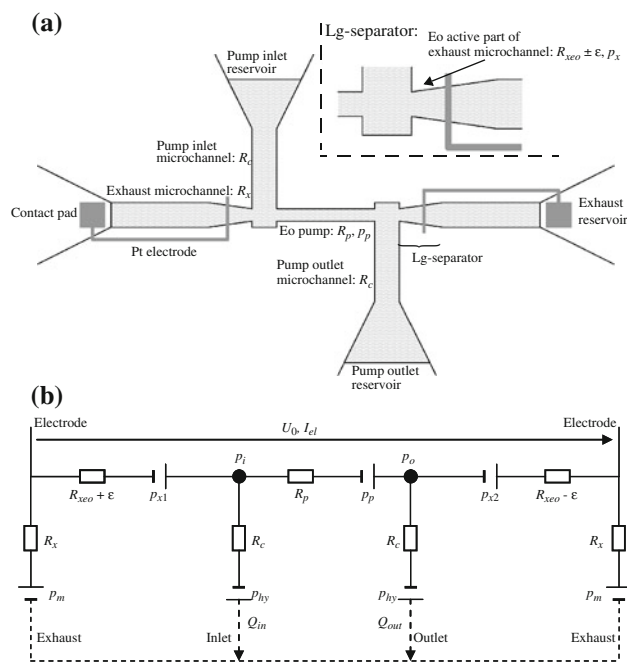

Fig. 9 a Schematic sketch of fluidic system including the eo pump with lg-separator. **b** Equivalent electrical circuit for the determination of flow and pressures within the fluidic system

inside the lg-separator. The layout of the eo pump, as shown in Fig. 9a, can be transformed into an equivalent electrical circuit, as shown in Fig. 9b. The flows and pressures within the eo pump can be determined by solving the equivalent electrical circuit diagram. The microchannels are replaced by resistors with a specific hydraulic resistance as described by Morf et al. (2001). R_c, R_p, R_x, denote the hydraulic resistance of the pump inlet and outlet, the eo pump, and the exhaust microchannel, respectively. The eo pressures are represented by voltage sources, p_p and p_x for the eo pump and the eo active part of the exhaust microchannel. This yields the following equations:

$$p_p = \mu_{eo}\rho_{el}R_pI_{el} \quad \text{and} \quad p_{x1,2} = \mu_{eo}\rho_{el}(R_{xeo} \pm \varepsilon)I_{el}, \quad (14)$$

where R_{xeo} represents the average hydraulic resistance of the eo active part of the exhaust microchannel and ε the difference in hydraulic resistance according to an alignment mismatch of the electrodes.

Furthermore, the hydrostatic pressure p_{hy} could have been integrated into the model as an initially charged capacitor. Its value represents the different filling levels in the reservoir of the pump inlet and outlet, as well as, an inclination of the chip. However, the consideration as a time independent voltage source p_{hy} simplifies the model and is a reasonable approximation since the displaced liquid volumes are small compared to the volume of the reservoir of about 0.2 μl. If, for example, both reservoirs are half filled, a displaced volume of 10 pl results in a hydrostatic pressure change of 1 μPa, which is negligible

compared to the experienced pressures within the fluidic system.

At the transition between the exhaust microchannel and the reservoir, a meniscus is formed, due to the sudden enlargement of the cross-section. The Young–Laplace pressure of this meniscus prevents a filling of the exhaust reservoir through the microchannel. The pressure drop over the meniscus is by an additional voltage source p_m. Without any voltage applied, water already evaporates from the meniscus, inducing an evaporation driven flow v. This evaporation driven flow defines the value of the voltage source $p_m = v(R_c + R_x)$ at $I_{el} = 0$. Once the pump is actuated, the shape of the meniscus adjusts according to the applied pressure at the exhaust microchannel outlet, which slightly changes the evaporation area, and thus the evaporation induced flow v.

Integrating all these effects leads to a definition of the Kirchhoff equations for the independent pressure at the pump inlet p_i and pump outlet p_o as:

$$\frac{p_i - p_{x1} - p_m}{R_x} + \frac{p_i + p_{hy}}{R_c} + \frac{p_i - p_o + p_p}{R_p} = 0$$
$$\frac{p_o - p_{x2} - p_m}{R_x} + \frac{p_o - p_{hy}}{R_c} + \frac{p_o - p_o - p_p}{R_p} = 0 \tag{15}$$

Solving this system of equations for p_i and p_o leads to the flow Q_{out} into the outlet microchannel and the flow Q_{in} into the inlet microchannel as:

$$Q_{out,in} = v \pm \frac{p_{hy} R_p R_x}{R_c \left[R_p R_x + R_c (R_p + 2R_x) \right]}$$
$$\pm \mu_{eo} \rho_{el} I_{el} \left(\frac{R_p (R_x - R_{x,incl})}{R_p R_x + R_c (R_p + 2R_x)} \mp \frac{\varepsilon}{R_c + R_x} \right). \tag{16}$$

Measuring Q_{out} and Q_{in}, and plotting it versus I_{el}, reveals the contributions from the evaporation induced flow v, the hydrostatic pressure induced flow p_{hy} and the flow induced by the misalignment of the electrodes ε. At $I_{el} = 0$ the evaporation induced flow v can be seen as the average offset of Q_{out} and Q_{in}:

$$\left. \frac{Q_{out} + Q_{in}}{2} \right|_{I_{el}=0} = v. \tag{17}$$

The hydrostatic pressure difference p_{hy} can be determined from the difference between Q_{out} and Q_{in}:

$$\left. \frac{Q_{out} - Q_{in}}{2} \right|_{I_{el}=0} = p_{hy} \frac{R_p R_x}{R_c \left[R_p R_x + R_c (R_p + 2R_x) \right]}. \tag{18}$$

The misalignment of the electrodes is expressed in the derivative of the average of Q_{out} and Q_{in} with respect to the current I_{el}:

$$\frac{d}{dI_{el}} \left(\frac{Q_{out} + Q_{in}}{2} \right) = \varepsilon \frac{\mu_{eo} \rho_{el}}{R_c + R_x}. \tag{19}$$

2.2.3 Dimensioning of the microchannels

The requirements on the design of the fluidic system were: a robust implementation regarding the manufacturing process and the actuation, and flows in the range of 10 pl s^{-1}, which amounts to an average velocity of 50 μm s^{-1} inside the pump outlet microchannel. For a sufficiently high aspect ratio (height to width) within the eo pump and the lg-separator, the deep reactive ion etching (DRIE) of the microchannels' height was targeted to be 10 μm in the widest microchannels. For the pump outlet and inlet, microchannels with a width of 20 μm were chosen. This led to a hydraulic resistance for a 800 μm long microchannel which was low compared to the hydraulic resistance of the eo pump. The eo pump had a width of 1.5 μm. This implied a trade-off between reliability during fabrication, appropriate pump backpressure p_b and sensitivity towards clogging. The minimum length of the pump is determined by the rounding of the corners during lithography and thermal oxidation. The minimum pump length was set to 30 μm, for a well-defined hydraulic resistance of the pump. In order to increase the flow, two of those pumps were connected in parallel, which halved the hydraulic and electrical resistance. The exhaust microchannel's width was designed to 20 μm and a length of 800 μm to reach the reservoir. This exhaust microchannel was placed at the outlet of the lg-separator. The design of the lg-separator was more complex. In order to have the highest backpressure p_b capacity of the lg-separator, an inlet width of 1.5 μm was chosen. The taper angle β was defined to reach a high backpressure p_b while maintaining at the same time the ability to reliably be defined during fabrication. During mask fabrication a tapered line was represented by a pixelated step-like profile with a minimum step size of 250 nm. These steps needed to be reliably smoothened out during lithography, DRIE and thermal oxidation. A safe choice seemed to be a taper angle of β = 11°, resulting in 39 steps over a length of 50 μm. In order to increase the reliability of lg-separator and to reduce the influence of the corner rounding, a 5 μm long microchannel was placed between the entrance of the lg-separator and the eo pump. Finally, the electrode was placed at a distance of 10 μm from the inlet of the lg-separator. This provided enough margin for a possible electrode misalignment. All this resulted in a complete footprint of 100 μm × 15 μm (length × width) of the eo pump.

3 Fabrication

3.1 Process flow

For the microfluidic system, microchannels with a constant height and variable width, and fluidic connections were
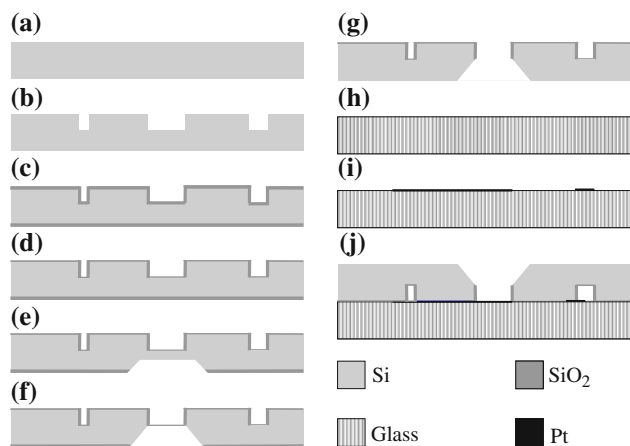
Fig. 10 Process flow for the integration of Pt electrodes into the microfluidic microchannels. **a** Double sided polished 525 μm wafer. **b** Outlining the microchannels as DRIE trenches. **c** Thermal oxidation in order to narrow down the width of the microchannels. **d** RIE to thin down the thermal oxide layer on the front surface for reliable bonding. **e** KOH etching the reservoirs as cavities from the backside of the wafer, stopping inside the Si. **f** Final etching of the cavities in TMAH for soft landing in SiO₂ membrane. **g** RIE from the backside to remove the SiO₂ for good electrical contact during anodic bonding and to remove the SiO₂ membrane inside the cavities for fluidic connection. **h** Boron type glass wafer for anodic bonding. **i** Lift-off metallization of 15 nm Ta and additional 150 nm Pt. **j** Anodic bonding of the two wafers to close the microchannels

required, as well as, electrodes inside the microchannels for eo, on-chip pumping. The process flow was based on photolithography, Si etching, thermal oxidation, lift-off metallization and anodic bonding for a two wafer process. A simplified process flow is shown in Fig. 10. (a) The first wafer was a double-side polished, 525 μm thick silicon (Si) wafer. (b) The microchannels were outlined by DRIE into the frontside of the wafer. The trench-width varied from 2 μm up to 20 μm with a depth of 10 μm for the 20 μm wide microchannel. (c) These microchannels were subsequently narrowed by thermally growing 1.5 μm of SiO_2, which reduced the initial width by 1.65 μm (55% of the SiO_2 grows out of the Si surface; Madou 2002). (d) As it turned out, a SiO_2 thickness of 1.5 μm was too thick for a reliable anodic bond, because of an insufficiently strong electrical field between the two wafers. Consequently, the SiO_2 surface was highly anisotropically thinned by reactive ion etching (RIE) to a final thickness of 100 nm, as suggested by Lee et al. (2000) and Plaza et al. (1998). Advantageous was also that more ions were implanted into the SiO_2, which further enhanced the bonding strength. (e) The fluidic connection to the chip was established by Si-wet-etching the reservoirs. These reservoirs were shaped as cavities through the wafer to also fluidically connect the backside to the frontside. The etching was performed from the backside through the wafer and stopped at the front side at the thin SiO_2 membrane. The Si-wet-etching was first

performed in potassium hydroxide (KOH) for a high etch rate and (f) then finished in tetramethylammonium hydroxide (TMAH) for a gentle stop at the SiO_2. This protected the SiO_2 frontside from being etched, in case a membrane broke. (g) Finally, the complete SiO_2 was removed from the backside by RIE to ensure a good electrical contact and to open the membranes for the fluidic connection. (h) The second wafer was a standard boron type glass wafer for anodic bonding. (i) The metallization of 15 nm tantalum (Ta) and 150 nm Pt was deposited in a lift-off process. (j) Both wafers were RCA[1] cleaned right before the anodic bonding process. The wafers were aligned in such a way that the microchannels ended in the fluidic connection. The wafers were anodically bonded at 400°C and an applied voltage of 1000 V for 1.5 h.

3.2 Fabrication results and discussion

The microchannel's dimensions were measured for accurately modeling the device. The first measurement determined the height of the microchannels. The well-known phenomena of an aspect ratio dependent etching for DRIE was investigated, the wider the opening, the faster the etch process (Madou 2002). It was necessary to extract the precise height of the microchannels with different widths from the test run. Figure 11a shows a cross-section of DRIE trenches with a width from 1 to 20 μm. 50 μm deep trenches were etched, where the etch depth was adjusted for the widest microchannel. Figure 11b shows the normalized etch depth with regard to the 20 μm wide microchannel. This can be used to determine the different microchannel heights of the fluidic system and, hence, their hydraulic resistance. Figure 12a shows two important results: the width of the eo pump and the rounding of the corners. The width of the eo pump can be determined to 1.5 μm. The intended width of 0.5 μm could not be reached probably due to widening during the DRIE. In future, this needs to be narrowed down in order to generate higher eo pump backpressures. The corners were initially rounded with a radius of 2 μm in the mask design to avoid stress concentrations and ensure repeatability in fabrication. The corner radius increased only up to 2.2 μm during fabrication. The cross-section of the microchannel was investigated by cutting it open, as shown in Fig. 12b. For a 20 μm deep and 4 μm wide microchannel, an inclination angle of the sidewall of 89° was measured, justifying the assumption of a rectangular microchannel cross-section. In addition, the 1.4 μm thick SiO_2 microchannel sidewall can be seen, indicated by the higher greyscale. Finally, the top corner of the microchannel rounded off during DRIE,

---

[1] $NH_4OH:H_2O_2:H_2O = 1:1:5$ at 70°C for 1 h.
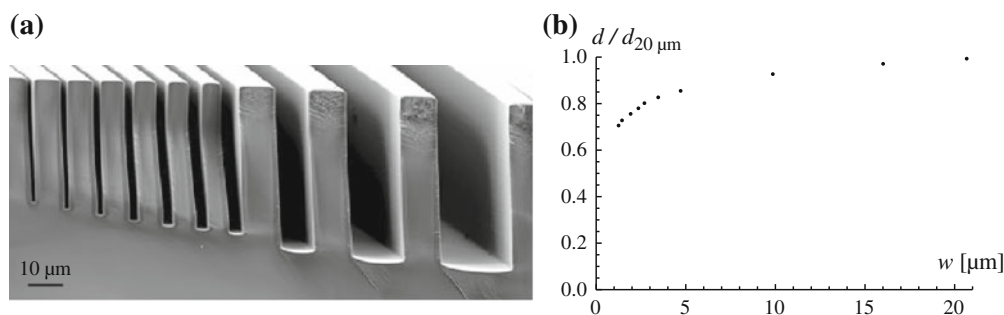
(a)

(b)

Fig. 11 **a** Scanning electron microscope (SEM) image showing that the depth of the DRIE trenches depended on the width of the microchannels. **b** The normalized depth with respect to a 20 μm wide microchannel, extracted from **a**
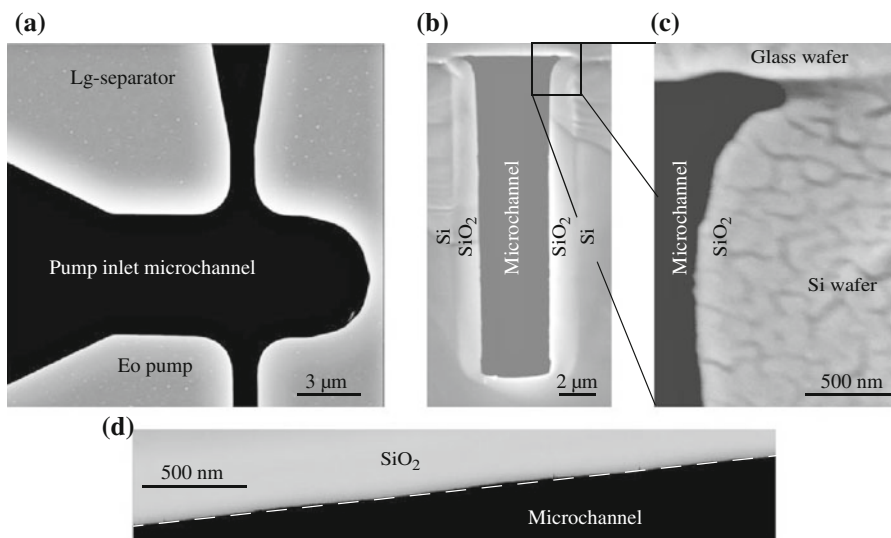
(a) **(b)** **(c)**

(d)

Fig. 12 SEM images of: **a** Top view of a DRIE and thermally oxidized pump inlet with the exhaust microchannel on the top and part of the eo pump at the bottom. The corners were rounded with a radius of 2.2 μm. The width of the eo pump was determined to 1.5 μm. **b, c** Shows a cross-section of pumping microchannel. **b** The sidewall of the microchannel deviated of about 1° from verticality.

The thermal oxide thickness can be determined to 1.4 μm. **c** The imperfection of the bonding on the top corner resulted in enhanced corner flow but has no major consequences during the actuation of the pump. **d** The stepping of the tapered sidewall of 5° resulted in a local variation of the taper angle $\beta \pm 0.6°$ after etching and thermal oxidation

thermal oxidation and RIE. The radius for this edge was measured to be 0.6 μm. After bonding, this recess resulted in a shallow 0.3 μm wide and 0.2 μm high additional microchannel, see Fig. 12c. This shallow part of the microchannel did not make a contribution to the hydraulic resistance but increased the cornerflow. A closer look was taken at the pixelation of the tapered sidewall to determine the minimum taper with acceptably rounded off steps. The problem with the pixelation of diagonal lines in the mask design is addressed in Fig. 12d. For a low taper angle β of 5°, only a slight deviation from the diagonal line of 20 nm per 1 μm long step was detected. This resulted in a local variation of the taper angle β of ±0.6°.

A result of the Pt lift-off process is shown in Fig. 13a. A triangle with an opening angle of 25° resulted in a curved

edge with a radius of 500 nm. This was a sufficiently small feature size, since the minimum Pt features in this design were 10 μm. However, the 185 nm thick Ta/Pt line had a strong influence on the bonding quality, as shown in Fig. 13b. It resulted in a non bonded area along the Pt line with a distance up to 25 μm away from the Pt edge. This non bonded area decreased the closer it reached the microchannel. Two effects can explain this void in the bond: the steric hindrance of the Pt line and the gas enclosure during the bonding step underneath the electrode. These gases, emerging during the bonding, were partially removed via the microchannels, which were connected to the outside. Applying a vacuum, in the range of 10 mbar, to support the extraction of this gas, did not increase the bonding quality. In this case, a plasma occurred between
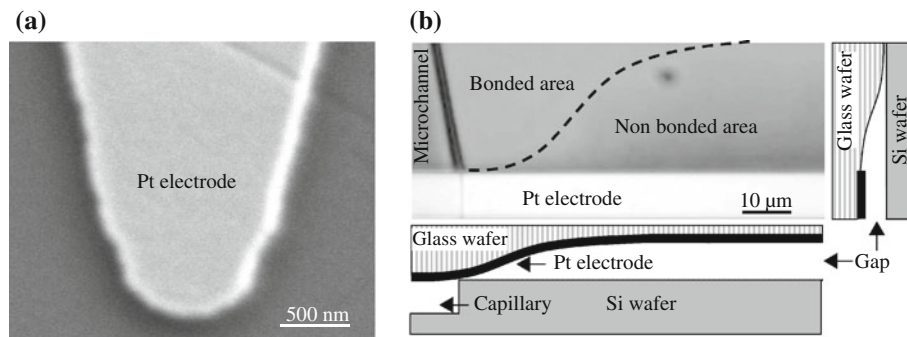
Fig. 13 a SEM image of a Pt lift-off fabricated tip with an opening angle of 25°. The tip rounded of with a radius of 500 nm, which defines a sufficient small feature size for the fabrication. b Optical microscope image of a non bonded area underneath the Pt electrode. This imperfection imposed a major reliability issue during actuation since hydrolysis can occur in this small gap and the emerging gases may leak into the pumping microchannel

Table 1 Dimensions fluidic system

Pump inlet/outlet microchannel	Height	10 µm	Width	20 µm	Length	800 µm
EO pump, two parallel microchannels	Height	7.5 µm	Width	1.5 µm	Length	30 µm
Lg-separator	Average height	8.8 µm	Inlet width/taper angle	1.5 µm/11°	Total length/electrode placement	50 µm/10 µm
Exhaust microchannel	Height	10 µm	Width	20 µm	Length	800 µm

the electrodes where the plasma current limited the applied voltage of the bonding setup to less than 1000 V. These gaps imposed a major drawback, not because of a liquid connection, since their hydraulic resistance was comparably high, but because hydrolysis occurred at higher currents in these gaps. These emerging electrolyzed gases escaped into the pumping microchannel. The microchannel dimensions after fabrication are summarized in Table 1.

4 Experiments, results, and discussion

In the first part of this section, the lg-separator for reliably venting the electrolyzed gases was investigated with respect to its backpressure p_b tolerance and its gas flow driving capability. In the second part, the eo pump was analyzed regarding to its linearity of the pump rate versus the electrical current, and the validity of the fluidic systems model. For each experiment, the chips were cleaned in an oxygen plasma for 20 min to remove any organic residues and to activate the SiO_2 surface. For the experiments the microchannels were filled with deionized water[2] having a specific resistivity of 12 MΩ cm. As flow marker a low concentration of 0.1 mM fluorescein[3] solution was employed.

4.1 Liquid–gas-separator

The first experiment verified Eq. 11, which states that the Young–Laplace pressure depends on the taper angle β. The experiment compared two taper angles $β_1$, $β_2$ by passively entrapping a gas bubble in a 10 µm deep microchannel with a maximum width at the meniscus of 5 µm. An optical image of the microchannel layout is shown in Fig. 14a. The microchannels were filled by water flowing in from the bottom and the air being pushed out of the system through the top. The flow split at the split-point into two independent flows. In the following section of the microchannel, it was important that the meniscus progressed with the same speed, until it reached the entrapment-point. From that moment onwards, the gas bubble was entrapped in the middle microchannel and compressed by the Young–Laplace pressure. After a certain time the bubble stayed at its equilibrium position, hence, the pressure inside the gas bubble was constant and must have matched the Young–Laplace pressure of the two entrapping menisci.

For a set of paired taper angles $β_1$, $β_2$ two different meniscus positions were investigated by entrapping two different volumes of air. For the analysis, the microchannels were filled and the images were taken immediately afterwards, in order to avoid the dissolution of air in water. According to Eq. 11, the Young–Laplace pressure was equal for both menisci in case their radius was equal. For the investigated taper angles β a good matching of the
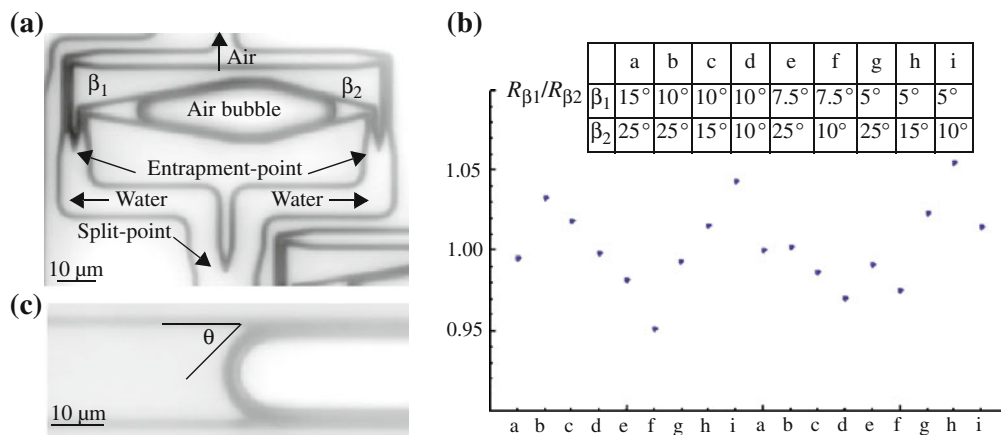
(a)

(b)

	a	b	c	d	e	f	g	h	i
β_1	15°	10°	10°	10°	7.5°	7.5°	5°	5°	5°
β_2	25°	25°	15°	10°	25°	10°	25°	15°	10°

(c)

Fig. 14 a Optical microscope image of an entrapped air bubble in tapered microchannel. b Ratio between the radii of two opposing meniscus in a microchannel with two different taper angles β_1 and β_2. Optical microscope topview image of the static contact angle $\theta_s = 45°$ inside the microchannel

Young–Laplace pressure of the two menisci can be concluded, as shown Fig. 14c. The Young–Laplace pressure was determined by taking an image from the topview and then fitting a radius to the meniscus. The ratio between the measured radii was 0.999, which was close to one representing a perfect matching. The standard deviation of this experiment was 0.026.

The static contact angle θ_s of water on SiO_2 inside the microchannel, as shown in Fig. 14c, was measured to be $\theta_s = 45°$ by fitting a radius to the meniscus and comparing it to the width of the capillary. The enhancement of the microchannel edges that can be seen in Fig. 14 could be interpreted as sign of corner flow, which would indicate a wetting angle smaller than 45° (Concus and Finn 1969). However, when looking at the cross-section of the channel in Fig. 12b and c, it becomes evident, that the small narrow spouts, a result of the bonding process, form a nano-capillary into which liquid enters and which are responsible for this contrast enhancement effect.

In order to calculate the maximum backpressure p_b of the lg-separator ($\beta = 11°$, $w_0 = 2.7$ μm, and electrode placement of $l_{ie} = 12$ μm from the inlet), the capillary Young–Laplace pressure p_1 of the first meniscus needed to be calculated. According to Eq. 11, the capillary pressure of the first meniscus was calculated to be $p_1 = 15$ kPa. The Young–Laplace pressure p_2 of the second meniscus in the exhaust microchannel needed to be assessed differently, since the exhaust microchannel had a cross-section with an aspect ratio of only 0.5. According to White (1999), the microchannel pressure of a rectangular cross-section can be estimated by substituting the radius of the meniscus by the hydraulic radius $r_h = A/s/\cos\theta_r$, where A is the cross-sectional area and s the wetted circumference. This leads to a Young–Laplace pressure p_2 of the second meniscus to $p_2 = 8$ kPa. Based on Eq. 13 the backpressure p_b of the lg-

separator can be calculated to $p_b = 7$ kPa. This defined its tolerance towards pressure changes which can be caused by contact angle changes due to contamination or cross-section changes.

Finally, the gas flow driving capability of the lg-separator integrated into the eo pump and the contact angle hysteresis within the exhaust microchannel was investigated, at a driving current of 20 nA and with using deionized water. Figure 15 shows three images, taken with a time difference of 7 s, of the emerging gas bubbles in the exhaust microchannel. Based on that, the flow of hydrolyzed gas was evaluated to be 2 pl s^{-1}. From 13 bubbles seen in these images, the receding contact angle $\theta_r = 42° \pm 3°$ and advancing contact angle $\theta_a = 47° \pm 4°$ of water on SiO_2 was determined in a similar way as described above for the static contact angle θ_s.

4.2 Electroosmotic flow determination

4.2.1 Experimental setup

For the eo induced flow determination, deionized water as the propelled liquid was chosen. Using deionized water resulted in a long Debye layer thickness λ_D on the SiO_2 surface, due to its low concentration of ions, see also Bruus (2008) for more information. This led to a high eo mobility μ_{eo} and, hence, to an enhanced flow. A drawback of the current design was that water evaporated out of the pumping microchannel's reservoirs during the experiment and, therefore, keeping a constant concentration of ions in the solution was impossible. The evaporation would have also concentrated any contaminations in the reservoir and the microchannels. In order to perform several measurements with the eo pump, the least contaminating solution, deionized water, was chosen. To trace the pumping action
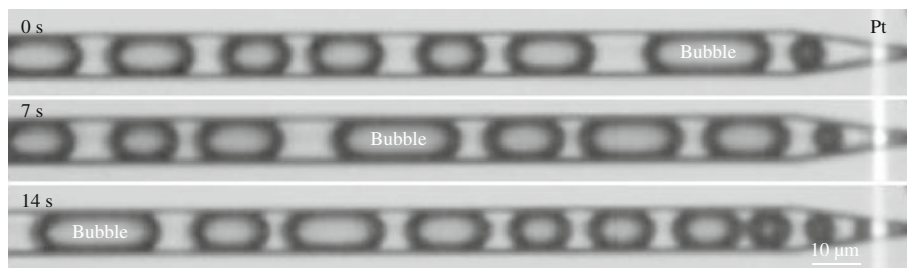
Fig. 15 Optical microscope image of an active lg-separator with a driving current of 20 nA. The time difference between the images was 7 s. The hydrogen evolution is estimated to generate a flow of 2 pl s^{-1}. In addition, the receding contact angle $\theta_r = 42° \pm 3°$ and advancing contact angle $\theta_a = 47° \pm 4°$ could be determined

inside the microchannel, a fluorescein solution was chosen. In these geometric dimensions and time frames, the fluorescein solution formed a clear meniscus, which was only slightly influenced by diffusion. The commonly used fluorescent labeled particles as a flow indicator were avoided since their interference with the high electric field (up to 0.2 MV m^{-1}) inside the eo pump was not clear. The pump was actuated in a way that the fluorescein solution never reached the eo pump in order to avoid any contamination in the eo active part.

For the experimental setup, the chip with the pump was placed on an inverted florescence microscope with a mounted CCD camera,[4] where the propagation of the fluorescein solution was monitored in a 400 μm long section of the pump outlet microchannel. The low concentration of fluorescein and the resulting low fluorescent emission allowed a maximum frame rate of 14 frames per second. Special attention was paid to the brightness and contrast settings. The greyscale inside the microchannel was chosen at a linear scaling from 0.15 up to 0.55 where 0.15 represented deionized water and 0.55, the fluorescein solution of 0.1 mM.

For the measurement, the electrodes were contacted via the contact pads inside the reservoirs of the exhaust microchannel. Then, a droplet of deionized water was dispensed into the reservoir of the pump inlet and finally, a droplet of fluorescein solution was filled into the reservoir of the pump outlet. A sequence of images was taken, as shown in Fig. 16, and analyzed according to the greyscale distribution in the center of the microchannel. A reference point, which was not affected by diffusion, needed to be found in order to follow the initial transition point between deionized water and fluorescein solution. Hence, it was assumed that the greyscale average between 0.55 and 0.15 represented half of the fluorescein concentration. In addition, the diffusion of fluorescein into deionized water and the diffusion of deionized water into the fluorescein

solution were assumed to be more or less the same at the low concentration used. Hence, a greyscale of 0.35 was not affected by diffusion and its progression in the center of the microchannel was considered as the location of the original interface and traced. Figure 16 shows a series of five consecutive greyscale distributions along the microchannel center. From this, the velocity v_{tp} of the transition point was obtained, which was then further transformed into the flow Q.

According to Bruus (2008), for a Poiseuille flow in a rectangular microchannel the velocity v_{tp} in its center can be described as:

$$
\begin{aligned}
v_{tp} &= \frac{4h^2\Delta p}{\pi^3 \eta L} \sum_{n,\text{odd}}^{\infty} \frac{1}{n^3} \left[1 - \frac{1}{\cosh\left(n\pi \frac{w}{2h}\right)} \right] \sin\left(\frac{n\pi}{2}\right) \\
&= \frac{48Q}{\pi^3(hw - 0.63h^3)} \sum_{n,\text{odd}}^{\infty} \frac{1}{n^3} \left[1 - \frac{1}{\cosh\left(n\pi \frac{w}{2h}\right)} \right] \sin\left(\frac{n\pi}{2}\right),
\end{aligned}
\tag{20}
$$

where the hydrostatic pressure Δp was replaced by $\Delta p = R_{hy}Q$ and the hydraulic resistance R_{hy} was calculated as $R_{hy} = 12\eta L/(h^3 w - 0.63\, h^4)$. Solving the sum numerically for the exhaust microchannel cross-section with $w = 2h$ yields the flow Q depending on the center velocity v_{tp} as:

$$
Q = \frac{h^2 v_{tp}}{0.9974}. \tag{21}
$$

4.2.2 Flow measurement and model verification

This subsection determines and compares the four flow contributions with the model: evaporation induced flow v, hydrostatic pressure p_{hy} induced flow, eo flow induced by the misalignment of the electrodes ε, and the intended eo flow. For the model validation, the solution's specific resistivity ρ_{el} and the eo mobility μ_{eo} needed to be experimentally defined. The solution's resistance was determined from Fig. 17a showing the current versus the potential applied between the bondpads

---

[4] Zeiss, Axiovert S40 with a mounted camera AxioCam Mrm and a metal halide lamp HXP 120.
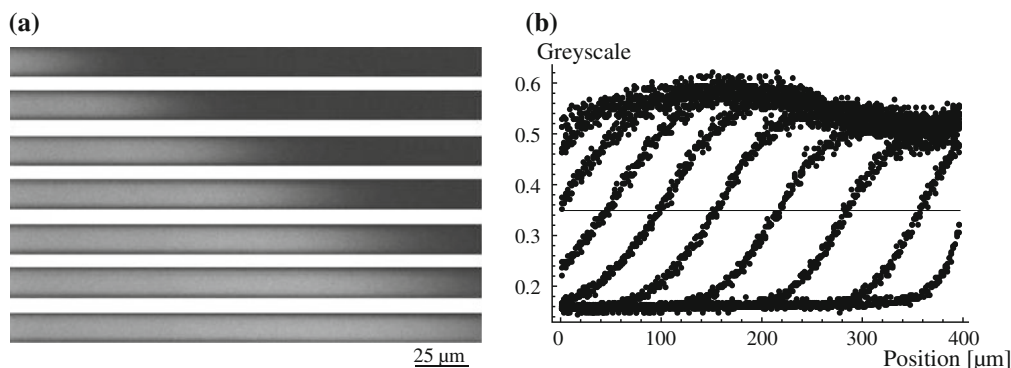
(a)

(b)

Fig. 16 **a** Fluorescent microscope image of the flow of fluorescein solution into the fluidic system replacing deionized water. Images taken with a time difference of 200 ms in a 400 μm long microchannel. **b** Greyscale distribution in the center of the microchannel deduced out of **a**
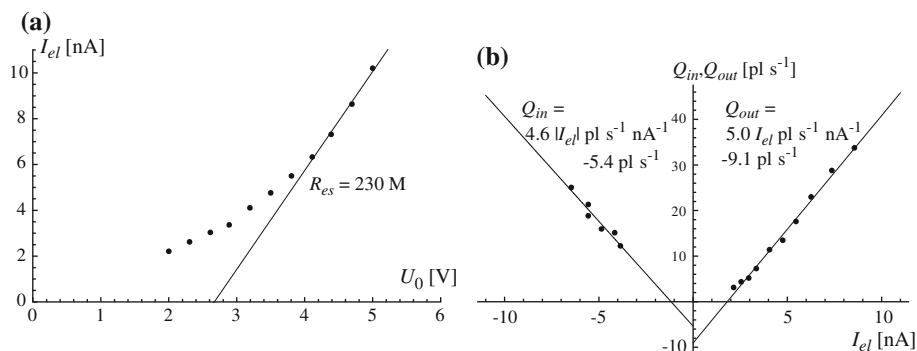
(a)

(b)

Fig. 17 **a** Voltage current curve of the eo pump. At low voltages the system is mainly determined by the current coupling of the electrode. The higher the applied voltage the higher the voltage drop over the fluidic system. The curve approaches the Ohmic behavior of the solution inside the fluidic system. **b** Current dependency of the flow into the eo pump Q_{in} and the flow out of the eo pump Q_{out}. At zero eo

current the median of the two flows was induced by evaporation through the exhaust microchannels. The difference between the two flows was induced by a hydrostatic pressure between the two reservoirs connected to the in and outlet of the eo pump. The different slopes of the flows were introduced by misalignment of the electrodes within the lg-separator

of the electrodes. The nonlinearity in this graph was caused by the current coupling of the electrode from the Pt into the solution. The consequence for the eo pump was, that for small currents, most of the potential drop occurred within the current coupling of the electrode and not over the eo pump. With higher currents, the electrical resistance of the eo pump became more dominant and, hence, most of the applied voltage dropped over the eo pump. This can also be seen, by the curve converging towards a linear, Ohmic behavior. To estimate the electrical resistance of the solution, the slope at a high potential, at 4.7 V, was determined. The electrical resistance of the solution was determined to be $R_{es} = 230$ MΩ. With the geometry, the specific resistance of the solution was calculated to be $\rho_{el} = 100$ Ωm. This was contradicting to the initial specific resistance of the deionized water, but could be explained by minute liquid volume inside the fluidic system, where already small saline contamination had a strong effect on the specific resistance. In order to understand this decreased specific resistance of the solution, the kind and concentration of contaminating ions was estimated. The source of the

contamination was speculated to be the residues of etching during fabrication and dissolved ions from the doped anodic bonding glass. Furthermore, the contamination is expected to be more of a saline character than an organic one, since the chips were cleaned in an oxygen plasma right before usage. Another observation supports this assumption, no local variations of the contact angle θ inside the microchannel were detected, which usually are a good indicator of organic contaminations. To assess the ionic concentration c of the contaminants, Kohlrausch's law and Ostwald's law of dilution was used. A solution's specific resistance of 100 Ω m can be reached with an ionic concentration of $c = 1$ mM, based on an average limiting molar ionic conductivity of 100 S cm^{-2} mol^{-1} for a saline contamination (alkali metals, values for the average taken from Coury (1999)). In other terms, to reach this ionic concentration a surface contamination in the range of 5 μmol m^{-2} was needed.

Knowing the ionic concentration c of the solution allowed to calculate the eo mobility μ_{eo}. The ionic concentration c led to a Debye layer thickness of $\lambda_D = 10$ nm

Table 2 Flows within the fluidic system

	Measured	Modeled	
Evaporation induced flow v	7.2 pl s^{-1}	7.4 pl s^{-1}	
Hydrostatic pressure p_{hy} induced flow	3.7 pl s^{-1}		p_{hy} = 1.7 Pa
Electrode misalignment ε induced flow	0.4 pl s^{-1} nA^{-1}	0.5 pl s^{-1} nA^{-1}	Misalignment 2 μm
Flow into eo pump Q_{ineo}	4.6 pl s^{-1} nA^{-1}	4.6 pl s^{-1} nA^{-1}	
Flow out of eo pump Q_{outeo}	5.0 pl s^{-1} nA^{-1}	5.1 pl s^{-1} nA^{-1}	

on a charged SiO_2 surface. The surface charge σ_{ch} at neutral pH values was determined by Zhou and Foley (2006) to σ_{ch} = 0.026 C m^{-2}. Finally, this can be used to estimate the eo mobility to μ_{eo} = 3 × 10^{-7} m^2 V^{-1}s^{-1}. These assumptions consider only bulk conduction, according to Stein et al. (2004) an enhancement of the conductance due to electroosmosis plays an important role in nanochannels. In their findings, conduction only determined by the bulk can be assumed at low saline concentrations c once: $w/\lambda_D \gg 1$ and $|\sigma_{ch}| \ll ecw$, where e represents the electron charge. In second case, of the surface charge σ_{ch}, this is at its limit and, hence, the concentration c might be slightly lower than estimated. Nevertheless, the values in this model are coarse estimations and treated as such, therefore, we do not expect a significantly different model. Moreover, the here derived values of the Debye layer thickness λ_D and the eo mobility μ_{eo} were in good correspondence with those given by Wang et al. (2006).

The experimental result for the flow Q_{out} out of the pump and the flow Q_{in} into of the eo pump are shown in Fig. 17b and summarized in Table 2. The evaporation induced flow v, was determined to be v = 7.2 pl s^{-1}, according to Eq. 17. The modeled value for evaporation induced flow was in the range of 7.4 pl s^{-1}. This value is based on the model developed in chapter 3, with an evaporation area of two times 9 × 20 μm at a temperature of 20°C and a relative lab humidity of 33%. The hydrostatic pressure p_{hy} induced flow was determined to be 3.7 pl s^{-1}, according to Eq. 18. The hydrostatic pressure p_{hy} was related to a height difference of the meniscus in the pump inlet reservoir with respect to the meniscus in the pump outlet reservoir. From Eq. 18 a hydrostatic pressure difference of p_{hy} = 1.7 Pa was calculated. This corresponds to a height difference of the meniscus in the inlet reservoir of 0.17 mm, lower than in the outlet reservoir. The misalignment of the electrodes was optically determined to be 2 μm into the exhaust microchannel of the pump inlet. The induced eo flow difference between Q_{out} and Q_{in} was determined to be 0.4 pl s^{-1} nA^{-1}, according to Eq. 19. Using the model and including the values for the specific resistance, the eo mobility μ_{eo} and a 2 μm

electrode misalignment led to an eo flow of 0.5 pl s^{-1} nA^{-1}. Finally, the general eo induced flow was determined to be Q_{ineo} = 4.6 pl s^{-1} nA^{-1} and Q_{outeo} = 5.0 pl s^{-1} nA^{-1}, which is in good agreement with the modeled values of Q_{ineo} = 4.6 pl s^{-1} nA^{-1} and Q_{outeo} = 5.1 pl s^{-1} nA^{-1}.

5 Summary and conclusion

To summarize, a successful analytically modeling and realization of an eo pump was shown. The novel approach of implementing a lg-separator, based on a tapered microchannel, allowed the current coupling from the Pt electrode into solution without mixing the emerging electrolyzed gases with the pumping liquid. Likewise, an easy fabrication technique based on a standard MEMS process and anodic bonding can be employed. All this resulted in an eo pump with a very small footprint of 100 μm × 15 μm (length × width) and an actuation with a low voltage, 2 V– 5 V.

The lg-separator had a maximum backpressure of 7 kPa and was able to reliably conduct away gas flows in the range of 2 pl s^{-1} generated at driving currents of up to 20 nA. The eo pump was modeled and measured. For deionized water, a flow out of the eo pump of Q_{out} = 5.0 pl s^{-1} nA^{-1} was achieved. At an applied voltage of 5 V, a current of 10 nA was measured which amounts to a flow of 50 pl s^{-1}. The developed model for the fluidic system also integrated effects like hydrostatic pressure and evaporation, as well as, fabrication imperfections like misalignment of the electrodes.

For a more detailed understanding of the electrode behavior a wider range of applied potentials is necessary. This would also allow a better prediction of the solutions specific conductivity and, hence, the eo mobility. In order to increase the backpressure of the eo pump an optimization can be achieved by connecting these pumps in series to obtain a multistage eo pump, as suggested by Takamura et al. (2003). Special attention needs to be taken in the design of the exhaust microchannels, since they will have to compensate for the increasing pressure between the

stages. Moreover, a promising direction for further investigation would be to specifically use the Pt electrodes as integrated electrochemical sensors by optimizing the microchannel design accordingly and removing the emerging gas bubbles respecting the model of the lg-separator.

References

Brask A, Kutter JP, Bruus H (2005) Long-term stable electroosmotic pump with ion exchange membranes. Lab Chip 5:730–738

Bruus H (2008) Theoretical microfluidics. Oxford University Press, Oxford

Concus P, Finn R (1969) On the behavior of a capillary surface in a wedge. Proc Natl Acad Sci 63:292–299

Coury L (1999) Conductance measurements part 1: theory. Curr Sep 18:91–96

Ghosal S (2004) Fluid mechanics of electroosmotic flow and its effect on band broadening in capillary electrophoresis. Electrophoresis 25:214–228

Guenat OT, Ghiglione D, Morf WE, de Rooij NF (2001) Partial electroosmotic pumping in complex capillary systems. Part 2: fabrication and application of a micro total analysis system (μtas) suited for continuous volumetric nanotitrations. Sens Actuators B 72:273–282

Guenther A, Jhunjhunwala M, Thalmann M, Schmidt MA, Jensen KF (2005) Micromixing of miscible liquids in segmented gas–liquid flow. Langmuir 21:1547–1555

Han A, Mondin G, Hegelbach NG, de Rooij NF, Staufer U (2006) Filling kinetics of liquids in nanochannels as narrow as 27 nm by capillary force. J Colloid Interface Sci 293:151–157

Hug TS, de Rooij NF, Staufer U (2005) Fabrication and electroosmotic flow measurements in micro- and nanofluidic channels. Microfluid Nanofluid 2:117–124

Jensen MJ, Goranovic G, Bruus H (2004) The clogging pressure of bubbles in hydrophilic microchannel contractions. J Micromech Microeng 14:876–883

Laser DJ, Santiago JG (2004) A review of micropumps. J Micromech Microeng 14:R35–R64

Lee TMH, Lee DHY, Liaw CYN, Lao AIK, Hsing IM (2000) Detailed characterization of anodic bonding process between glass and thin-film coated silicon substrates. Sens Actuators A 86:103–107

Madou MJ (2002) Fundamentals of microfabrication, 2nd edn. CRC Press, Boca Raton

Morf WE, Guenat OT, de Rooij NF (2001) Partial electroosmotic pumping in complex capillary systems. Part 1: principles and general theoretical approach. Sens Actuators B 72:266–272

Paust N, Litterst C, Metz T, Eck M, Ziegler C, Zengerle R, Koltay P (2009) Capillary-driven pumping for passive degassing and fuel supply in direct methanol fuel cells. Microfluid Nanofluid 7:531–543

Plaza JA, Esteve J, Lora-Tamayo E (1998) Effect of silicon oxide, silicon nitride and polysilicon layers on the electrostatic pressure during anodic bonding. Sens Actuators A 67:181–184

Seibel K, Schoeler L, Schaefer H, Boehm M (2008) A programmable planar electroosmotic micropump for lab-on-a-chip applications. J Micromech Microeng 18. doi:0.1088/0960-1317/18/025008

Stein D, Kruithof M, Dekker C (2004) Surface-charge-governed ion transport in nanofluidic channels. Phys Rev Lett 93. doi:10.1103/PhysRevLetter.93.035901

Takamura Y, Onoda H, Inokuchi H, Adachi S, Oki A, Horiike Y (2003) Low-voltage electroosmosis pump for stand-alone microfluidics devices. Electrophoresis 24:185–192

Wang P, Chen Z, Chang HC (2006) A new electro-osmotic pump based on silicamonoliths. Sens Actuators B 113:500–509

White FM (1999) Fluid mechanics, 4th edn. McGraw-Hill, New York

Zhou MX, Foley JP (2006) Quantitative theory of electroosmotic flow in fused-silica capillaries using an extended site-dissociation-site-binding model. Anal Chem 78:1849–1858